NANO LETTERS

pubs.acs.org/NanoLett Letter

Spectrally Tunable Ultrafast Long Wave Infrared Detection at Room Temperature

Tianyi Guo, Sayan Chandra, Arindam Dasgupta, Muhammad Waqas Shabbir, Aritra Biswas, and Debashis Chanda*

Cite This: https://doi.org/10.1021/acs.nanolett.4c03832 Read Online

ACCESS | Metrics & More | Article Recommendations | Supporting Information

ABSTRACT: Room-temperature longwave infrared (LWIR) detectors are preferred over cryogenically cooled solutions due to the cost effectiveness and ease of operation. The performance of present uncooled LWIR detectors such as microbolometers, is limited by reduced sensitivity, slow response time, and the lack of dynamic spectral tunability. Here, we present a graphene-based efficient room-temperature LWIR detector with high detectivity and fast response time utilizing its tunable optical and electronic characteristics. The inherent weak light absorption is enhanced by Dirac plasmons on the patterned graphene coupled to an optical cavity. The absorbed energy is converted into photovoltage by the Seebeck effect with an asymmetric carrier generation environment. Further, dynamic spectral tunability in the 8−12 μm LWIR band is achieved by electrostatic gating. The proposed detection platform paves the path to a fresh generation of uncooled graphene-based LWIR photodetectors for wide ranging applications such as molecular sensing, medical diagnostics, military, security and space.

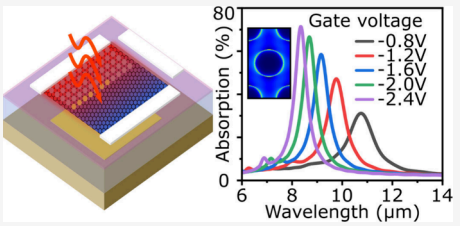

KEYWORDS: *infrared detector, graphene, two-dimensional materials, Dirac plasmons, photothermoelectric effect*

Longwave infrared (LWIR) detectors, operating in the 8 to 12 μm wavelength range, have diverse applications in night vision, space exploration, surveillance, thermal imaging and defense related applications.[1−5] However, LWIR detection at room temperature is challenging due to the low photon energy and high background noise. Therefore, cryogenic cooling is required for sensitive LWIR detectors to achieve optimal detectivity.[6,7] There is a growing demand in developing efficient room-temperature LWIR detectors for their low cost and ease of operation. However, uncooled microbolometers such as vanadium penta-oxide (V_2O_5) and amorphous silicon (a-Si) based detectors suffer from lower sensitivity (D* ~ 10^8) and slow response time (10s ms).[5,8,9] Furthermore, due to their inherent broadband absorption, both cryo-cooled detectors and uncooled microbolometers lack the capability of spectral tunability. While the use of tunable IR filters based LWIR detection can offer spectral tenability,[10,11] their performance is compromised notably in terms of detectivity. Spectrally tunable LWIR detectors have gained huge interest for their potential in various applications such as precise material identification, selective gas sensing, advanced spectroscopic analysis, tailored remote sensing and hyper-spectral imaging. Hence, it is imperative to investigate materials and techniques that facilitate the creation of LWIR detectors operating at room temperature with exceptional detectivity, fast response time, and the ability to dynamically tune their operational wavelength.

The emergence of CVD grown large area graphene, has unlocked great potential for sensitive and fast LWIR detection with its unique Dirac cone band structure, high carrier mobility, and distinctive thermal properties.[12,13] Furthermore, electrostatic gating enables tailored electronic and optical properties in graphene, allowing for dynamic spectral tenability.[14−17] However, the intrinsic absorption of LWIR radiation in graphene is as low as 2.3% due to its one-atom thickness and low carrier concentration. Prior research has investigated diverse approaches to enhance the light absorption in graphene, including employing additional layers of plasmonic structures and patterning the graphene itself.[18,19] Patterning graphene directly offers several advantages like seamless integration and increased versatility. Another major challenge in developing an efficient LWIR detector with graphene is achieving effective electrostatic gating for dynamic tunability. The commonly used top or bottom gate geometry has limitations that either obstruct the incident light or prevent the creation of an optical cavity. Instead, a side gate allows direct light access to the graphene layer. In recent years, the use of ion gel as an efficient gate dielectric has enabled the fabrication of large-area graphene-based field-effect transistor (FET) optical devices.[20−22] Ion gel, composed of a polymer matrix infused with an ionic liquid, offers high gate capacitance

Received: August 8, 2024
Revised: October 31, 2024
Accepted: November 1, 2024

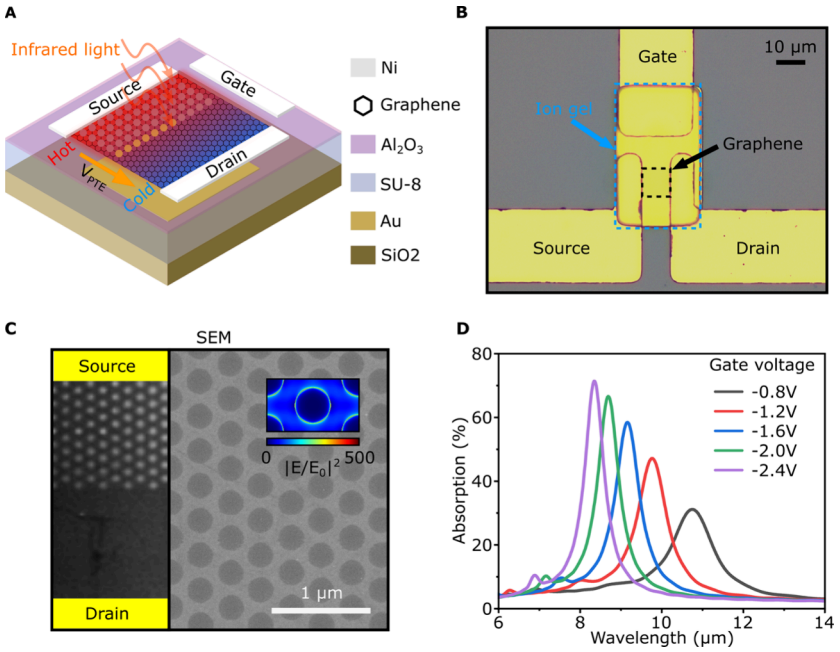

Figure 1. Dynamically tunable graphene based LWIR detector architecture. (A) Schematic illustration of the detector, with infrared illumination, a temperature gradient is created in the graphene channel, leading to the photothermoelectric voltage V_{PTE}. (B) Optical microscope image of the detector. The ion gel region (blue dashed line) and graphene region (black dashed line) are highlighted. (C) SEM image of the asymmetrically patterned graphene and the corresponding zoomed-in view shows the hexagonal hole array pattern with diameter D = 400 nm and period P = 600 nm. The inset depicts a simulated electric field profile at the localized surface plasmon resonance of the patterned graphene (λ = 8.35 μm), showing the maximum electric field intensity at the edges of the circular nanoholes. (D) Simulated absorption spectra of the cavity-coupled graphene patterned with holes in a hexagonal array, shown as a function of the applied gate voltage.

and ionic conductivity, enabling dynamic control of the Fermi level of graphene over a large area with low gate voltage. A type of ion gel with thin layer thickness, transparency to LWIR radiation and compatibility with photolithography has been developed; moreover, the stability of such ion gel can be substantially enhanced.[23] Therefore, ion gel gating provides immense potential for developing graphene based LWIR detectors. While ion gel-gated optical devices with graphene have been demonstrated, there is currently no demonstration of their application in LWIR detection.

Here, we present a room-temperature LWIR detector utilizing ion gel-gated monolayer graphene, which exhibits dynamically tunable spectral response. By patterning the graphene into a cavity-coupled hexagonal-hole array, we achieve an enhanced absorption of ∼70% by exciting Dirac localized plasmons which is further electrostatically tunable within the LWIR spectra range. A carrier temperature gradient is induced in the graphene layer through absorption asymmetry, by patterning half of it with a hexagonal-hole array and leaving the other half unpatterned. The detection relies on photothermoelectric effect to convert the asymmetry of carrier temperature into an electrical signal.[24−26] The preliminary detector demonstrates a unique dynamic spectral tuning ability from 8.5 to 11.2 μm while reaching a maximum detectivity of 3.15 × 10^9 Jones at an ultrafast response time of 144 ns, surpassing the capabilities of the conventional uncooled microbolometers by several orders of magnitude. This demonstration underscores the potential of engineered monolayer graphene LWIR detectors operating at room temperature, offering high sensitivity as well as dynamic spectral tunability for spectroscopic imaging.

The architecture of the LWIR detector based on large area CVD grown graphene is depicted in Figure 1A. The design comprises a 10 × 10 μm^2 monolayer graphene channel coupled to an optical cavity. Upon LWIR illumination, the coherent interaction between the optical cavity mode and the Dirac localized plasmons on the patterned graphene substantially enhances LWIR absorption in the nanopatterned graphene (NPG) layer by about 30 times. A 3-terminal field effect transistor (FET) is formed on the graphene electrodes as shown in Figure 1A. An electrical bias to the graphene channel is provided by the source and drain electrodes. The gate electrode is fabricated by the side of graphene. A thin ion gel layer is used as the gate dielectric. The carrier concentration in the NPG is dynamically tuned by varying the gate voltage. Figure 1B shows the microscopic image of the fabricated detector. Details of the device fabrication are included in the Supporting Information. A scanning electron microscope (SEM) image in Figure 1C shows the half-patterned graphene with circular holes of 400 nm diameter in a hexagonal array of 600 nm period. The proposed detector converts the absorbed light to electrical signal through Seebeck effect. When exposed to light, localized surface plasmons (LSP) are generated in the patterned side near the edge of the holes. The LSP eventually dissipates its energy through various damping pathways in graphene such as phonon emission, bulk scattering, and resistive loss can be prominent.[27,28] However, the dominant damping pathway is the edge-assisted Landau scattering leading to hot carrier generation in the patterned region, while the lattice temperature remains unaffected due to the slower lattice heating time.[12] For the unpatterned half, it exhibits low absorption of approximately 2%. Therefore, the carrier temperature is hardly affected. The Seebeck effect rises from the asymmetry of carrier temperature between the patterned and the unpatterned half of the graphene.[29] The diffusion of the hot carriers from the hot-end to the cold-end

https://doi.org/10.1021/acs.nanolett.4c03832
Nano Lett. XXXX, XXX, XXX−XXX

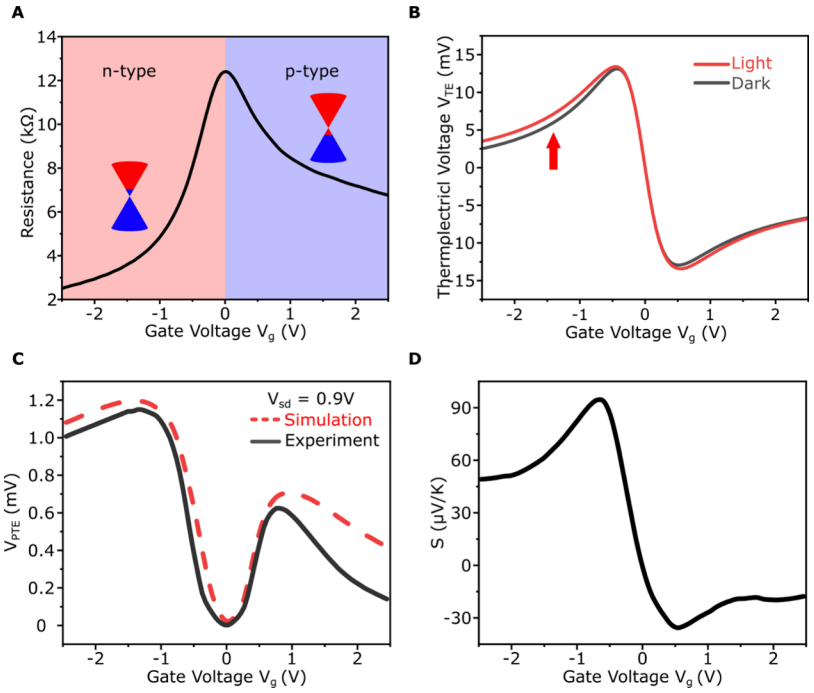

Figure 2. Dynamic doping. (A) Change of carrier concentration measured as resistance change of the asymmetrically patterned graphene as a function of the gate voltage (V_g) at a constant source−drain voltage (V_{sd}) of 0.9 V. (B) Thermoelectric voltage (V_{TE}) measurements corresponding to illumination with a blackbody light source and dark conditions plotted as a function of the gate voltage at the same V_{sd} of 0.9 V. (C) Comparison between simulated and experimental photoinduced thermoelectric voltage (V_{PTE}) as a function of gate voltage. (D) Gate voltage dependence of the Seebeck coefficient, deduced from the resistance vs V_g measurement.

creates a photothermoelectric voltage across the source-drain electrodes.[30,31]

For efficient detection, the hot carriers need to be collected before transferring their energy to the lattice. Therefore, the channel length of the NPG is designed to be 10 μm, which is shorter than the hot carriers' diffusion length estimated to be ~12 μm[12]. Figure 1D shows the dynamic tuning of the absorption spectra of the patterned graphene within the 6 to 14 μm as a function of gate voltage. By increasing the gate voltage, the Fermi level of graphene is elevated, resulting in a higher carrier concentration and longer carrier lifetime due to the increase in density of states. This leads to increased conductivity, a stronger plasmonic response, and enhanced peak absorption. Conversely, decreasing the gate voltage reduces the response. The shift in localized surface plasmon resonance (LSPR) frequency with Fermi energy can be expressed by

$$\omega_{LSPR} \propto \sqrt{\frac{CE_F}{d}} \tag{1}$$

where ω_{LSPR} is the localized surface plasmon resonance frequency, d is the edge-to-edge distance of the adjacent antidisks, E_F is the Fermi energy of the graphene, and C is the eigenvalue of the total electric potential equation. Based on this equation, the elevated Fermi energy caused by a high gate voltage leads to an increased LSPR frequency thus the absorption peak blueshifts.[17,32] It is worth noting that the absorption peaks exhibit a smaller full width at half-maximum (FWHM) with a higher gate voltage, due to the longer carrier lifetime at high Fermi energy. The maximum absorption of 70% occurs at a wavelength of 8.3 μm for a gate voltage of −2.4 V, corresponding to the Fermi level of E_F = 1 eV. The overlay of the electrical field in Figure 1C illustrates the finite difference time domain (FDTD) predicted electrical field on the surface of the graphene at Fermi level E_F = 1 eV. It can be clearly observed enhancement of the electrical field at the edge of the circular nanohole patterns.

Figure 2A shows the gate-dependent resistance change. The n-type and p-type doping regions highlighted with a red/blue background. The insets of Figure 2A schematically show the band diagrams of graphene corresponding to both p- and n-type doping. All the measurements are performed at room temperature. Here, the gate voltage V_g is expressed as $V_g = V_{gexp} - V_{CNP}$, where V_{gexp} is the applied gate voltage, V_{CNP} is the specific gate voltage where the charge-neutral point (CNP) of the graphene is found. With pristine graphene, CNP is expected to occur at V_{CNP} = 0. However, slight doping is common in CVD-grown and wet-transferred graphene due to defects and impurities introduced by various experimental conditions.[33−35] Thus, V_{CNP} is often found to be non-zero. Therefore, V_g instead of V_{gexp} is used in the figures to present n-type and p-type doping better. For V_g < 0, graphene undergoes n-type doping, while V_g = 0 corresponds to a charge-neutral point, and V_g > 0 leads to p-type doping in graphene. Figure 2A shows a 4-fold resistance change between V_g = 0 and V_g = −2.4 V in the n-type doping region, while a 2-time resistance change is found with the p-type doping region. This asymmetry can be attributed to the difference in electron and hole mobilities.[36−38]

First, the photoresponse from the detector is characterized by illuminating it with a blackbody light source and incident power of P_{in} = 153 nW. Figure 2B illustrates the changes in the thermoelectric voltage (V_{TE}) of the graphene detector with varying gate voltage under blackbody light source (red) and dark (blue) conditions. The graphene channel is driven with a constant bias voltage of V_{sd} = 0.9 V between the source and the

https://doi.org/10.1021/acs.nanolett.4c03832
Nano Lett. XXXX, XXX, XXX−XXX

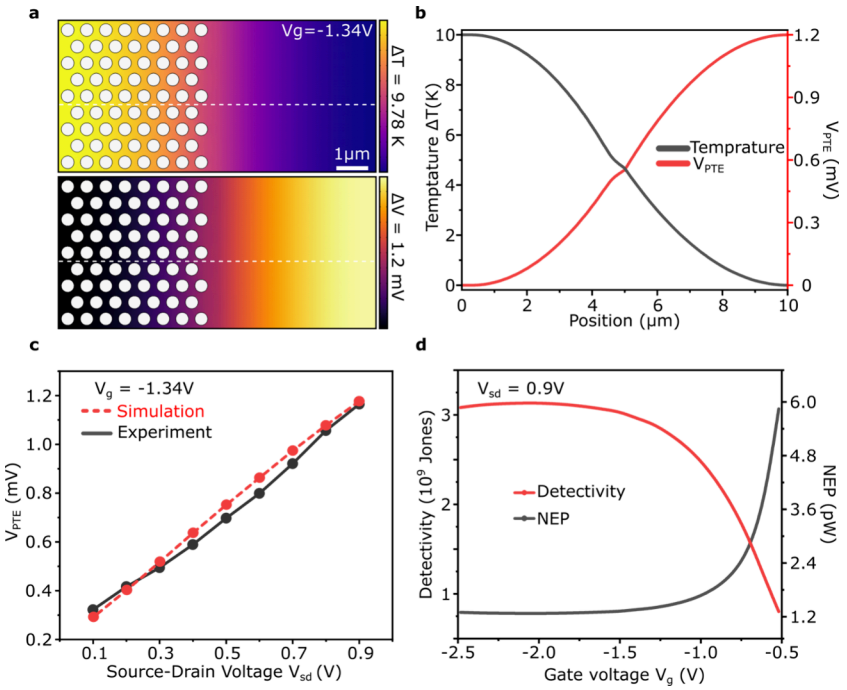

Figure 3. Hot carrier separation and generation of photothermoelectric voltage. (A) Distribution maps of carrier temperature (top) and corresponding photothermoelectric potential (bottom) across the asymmetrically patterned graphene channel at $V_g = -1.34$ V. (B) Line-cut plots presenting the variation in carrier temperature and photothermoelectric voltage along the graphene channel. (C) Change of photothermoelectric voltage (V_{PTE}) as a function of source-drain voltage (V_{sd}) at a constant $V_g = -1.34$ V. (D) The effect of gate voltage on the detectivity (D*) and noise equivalent power (NEP) at an optimum $V_{sd} = 0.9$ V.

drain. No hysteresis was found in the device as indicated in Supporting Information Figure S5 with a forward and backward V_{sd} sweeping. The photothermoelectric voltage (V_{PTE}) is further extracted by subtracting the recorded V_{TE} values in light and dark conditions. The experimentally measured V_{PTE} (black) along with the simulated V_{PTE} (red dashed) as a function of the gate voltage is plotted in Figure 2C which shows a good agreement. More details about the calculation of V_{TE} and V_{PTE} are described in the Supporting Information. Although, the highest absorption occurs at the largest gate voltage $V_g = -2.4$ V (Figure 1D), the largest V_{PTE} is observed at a lower gate voltage $V_g = -1.4$ V. This can be explained by the origin of the photothermoelectric voltage from the Seebeck effect. The photothermoelectric voltage (V_{PTE}) can be mathematically represented as the integral of the Seebeck coefficient ($S(x)$) multiplied by the gradient of carrier temperature ($T_{carrier}$) which depends on the absorption with respect to the position (x) of the graphene film, ranging from the position of the electrical contact on the patterned graphene side (X_p) to the position on the unpatterned graphene side (X_u):

$$V_{PTE} = \int_{X_p}^{X_u} S(x) \frac{\partial T_{carrier}(x)}{\partial x}\, dx \tag{2}$$

Figure 2D plots the Seebeck coefficient S of the graphene film, which is extracted from the resistance-vs-gate voltage measurement[12,25] in Figure 2A with the Mott relation as

$$S = \frac{\pi^2 k_B{}^2 T}{3e} \frac{\partial \ln \sigma}{\partial E_F} \tag{3}$$

where σ, k_B, and e are electrical conductivity, Boltzmann constant, and electron charge, respectively. Here, E_F is related to the applied gate voltage by $E_F = \hbar v_F (\pi C V_g/e)^{1/2}$, where 10^6 ms^{-1} is the Fermi velocity of the charge carriers in graphene and C is the capacitance of the ion-gel gating medium. It can be observed that the V_g with the highest Seebeck coefficient is reached at $V_g = -0.75$ V. Figure 2C shows the combined impact of $T_{carrier}(x)$ and S to the photoresponse with respect to the gate voltage.

The experimental findings are compared with the finite element simulations using COMSOL Multiphysics. In the simulation, a constant source-drain voltage of $V_{sd} = 0.9$ V, and an incident LWIR radiation power of 153 nW are maintained. The top image in Figure 3A illustrates the distribution map of the carrier temperature across the half-patterned graphene channel, revealing a temperature difference of $\Delta T = 9.78$ K compared to the coolest region in the unpatterned graphene with a gate voltage of $V_g = -1.34$ V. The corresponding potential distribution map is displayed in the bottom image of Figure 3A, demonstrating that the carrier temperature difference results in a photothermoelectric voltage of 1.2 mV. Furthermore, Figure 3B presents line plots depicting the variation of carrier temperature and photothermoelectric voltage along the graphene channel in the temperature and potential maps, respectively. A clear trend is evident: as we move along from the patterned half to the unpatterned half, the carrier temperature decreases, while the photothermoelectric voltage increases. To investigate the correlation between the V_{PTE} and the source-drain voltage (V_{sd}), we keep the gate voltage fixed at $V_g = -1.34$ V while varying V_{sd} from 0 to 0.9 V. Both the experimental and simulation results, shown in Figure 3C, indicate a clear linear relationship between V_{PTE} and V_{sd}. This behavior can be attributed to the increased diffusion of hot carriers facilitated by higher bias voltages. Although, a higher V_{sd} leads to higher V_{PTE}, it is observed in the experiment

https://doi.org/10.1021/acs.nanolett.4c03832
Nano Lett. XXXX, XXX, XXX−XXX

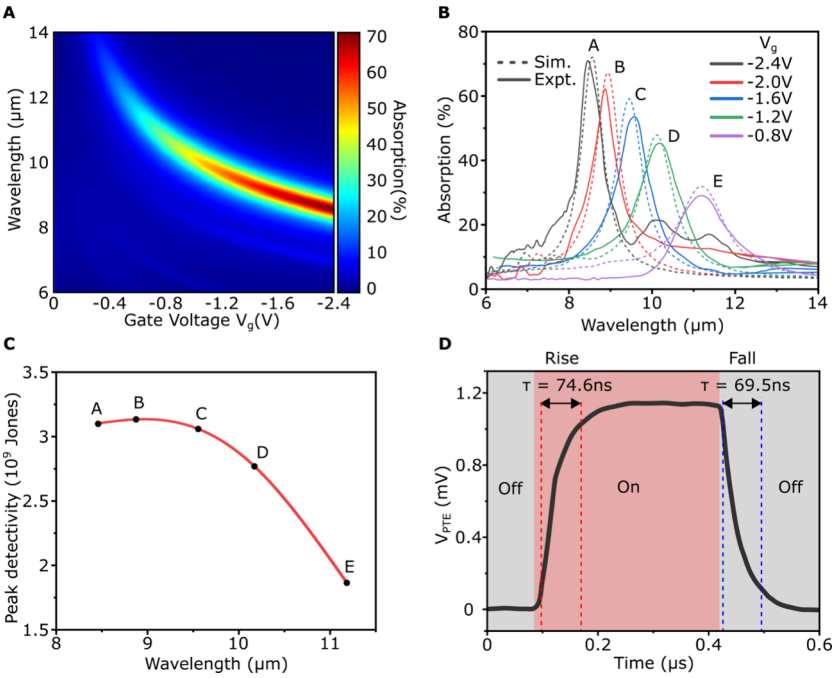

Figure 4. Spectrally tunable LWIR detection. (A) Simulated contour plot depicting the evolution of the absorption peak of the hexagonal hole array patterned graphene as a function of gate voltage. (B) Comparison of the experimentally measured (solid) and simulated (dashed) absorption spectra of the patterned graphene at certain gate voltages and the corresponding measured peak detectivity for a constant V_{sd} = 0.6 V is shown in (C). (D) Time response measurement of the graphene detector showing an ultrafast response time of $\tau \sim 144$ ns.

that a V_{sd} of more than 1 V affects the stability of the graphene detector under constant operation. Thus, a source-drain voltage of 0.9 V is used in experiments.

In order to evaluate the LWIR detector's performance, we conducted measurements on its dynamic tunability of detectivity, denoted as D*. Figure 3D plots D* and the noise equivalent power (NEP) with respect to the gate voltage. The measurement setup is illustrated in the Supporting Information Figure S4. The D* is defined by the expression:

$$D^* = \sqrt{A}/NEP \tag{4}$$

where, A is the active area of the detector and NEP is the noise equivalent power. The NEP can be determined by

$$\mathrm{NEP} = S_n/\mathcal{R} \tag{5}$$

where Sn is the noise spectral density. The Sn vs gate voltage Vg is shown in Supporting Information Figure S6 and Figure S7. The Sn with different frequencies at Vg = −2.0 is shown in Figure S7. The responsivity $\mathcal{R}$ can be determined as follows:

$$\mathcal{R} = V_{PTE}/P_{\mathrm{inc}} \tag{6}$$

where P_{inc} is the incident power on the active region of the device. The highest detectivity of 3.15×10^9 Jones is measured at a gate voltage of −2.0 V with a responsivity of 6.99×10^3 V/W. Both the responsivity (6.99×10^3 V/W) and detectivity (3.15×10^9 Jones) is higher when compared with other graphene-based room temperature LWIR detectors[39−41] (2.8×10^3 V/W and 1.1×10^9 Jones). The responsivity at different incident power is shown in Supporting Information Figure S8. It is worth noting that the detectivity of the graphene detector exhibits a plateau over a wide range of gate voltage V_g between −2.5 V and −1.5 V, which defines the optimum range of operation.

Next, we examined the dynamic spectral tunability of the monolayer graphene-based room temperature LWIR detector. The correlation between the peak absorption wavelengths of the detector and the applied gate voltage is simulated using Finite-Difference Time-Domain (FDTD) simulation. The contour plot in Figure 4A shows the evolution of the absorption wavelength as a function of the gate voltage. Furthermore, in Figure 4B, the experimentally measured absorption spectra (solid) for different gate voltages are compared with the FDTD simulation results (dashed). It is evident that a broad tuning range of 2.7 μm for the center wavelength is achieved, spanning from approximately 8.5 to 11.2 μm. The comparison of the absorption between the patterned graphene and unpatterned graphene is shown in Figure S1. The absorption of the graphene device was taken with a reference spectrum of the SU-8/Al_2O_3 layer. The presence of the SU-8 cavity causes a loss in absorption as shown in Figure S2. Exploring cavity materials with more transparency would increase the performance of the proposed detector. Figure 4C illustrates the peak detectivities at the selected gate voltages plotted against the corresponding peak absorption wavelengths. The peak detectivity is obtained by the incident power from the blackbody source radiation within the $1/e^2$ width of the absorption peak. The radiation spectrum of blackbody source can be found Figure S3. While the detectivity represents the performance of the graphene detector in the whole 8−12 μm wavelength range, the peak detectivity stands for the performance of the detector at the selected operational wavelength range. This further demonstrates the dynamic spectral tunability of the graphene-based room temperature LWIR detector across the atmospheric transparent window. The time response of the proposed detector is measured by recording the rise time τ_{rise} and fall time τ_{fall} during the switching between dark-to-light and light-to-dark conditions, respectively. τ_{rise} and τ_{fall} are calculated by

https://doi.org/10.1021/acs.nanolett.4c03832
Nano Lett. XXXX, XXX, XXX−XXX

the time duration between 10% and 90% of changes between the steady-state voltages. The total time response of the detector is further expressed as $\tau_{total} = \tau_{rise} + \tau_{fall}$.

Figure 4D plots the experimental data of the time response measurement, where we record a τ_{rise} = 74.6 ns and τ_{fall} = 69.5 ns indicating a response time of τ_{total} = 144 ns. It should be noted that the response time of our detector is only limited by the experimental setup. The response time can be further reduced as the Dirac plasmon relaxation lifetime is less than 1 ps.[12,42]

This response time of ∼144 ns is three-orders of magnitude faster compared to the uncooled bolometers which are typically limited to the microsecond response time. High sensitivity (D* > 10^9), fast response time (τ < 150 ns) and dynamic spectral tunability at room temperature make this proposed detector distinguished from the present technologies. Table 1 includes the performance comparison in responsivity,

Table 1. Performance Comparison between Different LWIR Detectors

	Operation condition	Detectivity (Jones)	Dynamic spectral tunability	Response time
Bolometers[2]	Room temperature	∼10^8	No	>7 ms
Quantum well infrared photodetectors	Cooled	∼10^{10}	Yes	∼ps
MCT photodetectors[2]	Cryogenic cooling	10^9–10^{11}	No	<10 ns
Other graphene-based detectors[39−41]	Room temperature	<1.2 × 10^9	No	4 ns–8 μs
This work	Room temperature	3.15 × 10^9	Yes	144 ns (Circuit limited)

detectivity and response time between the various LWIR detection technologies and the detector in this work. The device life is characterized and shown in the Supporting Information Figure S9.

In conclusion, we have successfully demonstrated a room-temperature LWIR detector with dynamic spectral tunability with cavity-coupled nanopatterned monolayer graphene. This detector showcased exceptional performance, with a high detectivity of 3.15 × 10^9 Jones and a fast response time of 144 ns, surpassing the capabilities of conventional uncooled microbolometers by several orders of magnitude. It paves the way for low-cost, sensitive, and fast infrared detection at room temperature. Importantly, our detector provides the advantage of dynamically tuning the spectral response by selectively targeting operational wavelengths within the LWIR range of 8 to 14 μm, which is missing in both traditional cryogenically cooled LWIR photodetectors and bolometers. The versatility of our approach opens up exciting possibilities for a wide range of applications, including thermal imaging, night vision, and material identification. Overall, our work represents a step forward in the development of advanced room-temperature LWIR detection technology with broad implications in various fields.

■ ASSOCIATED CONTENT

Data Availability Statement

All data needed to evaluate the conclusions in the paper are present in the paper and/or the Supporting Information.

Supporting Information

The Supporting Information is available free of charge at https://pubs.acs.org/doi/10.1021/acs.nanolett.4c03832.

Supporting Information Figure S1: Absorption comparison between patterned and unpatterned graphene. Supporting Information Figure S2: SU-8 + Al_2O_3 cavity absorption. Supporting Information Figure S3: Emission spectrum of the blackbody source at 1060 °C. Supporting Information Figure S4: Optical setup for the electrical measurements with blackbody source. Supporting Information Figure S5: I−V curve with forward and backward voltage sweeping. Supporting Information Figure S6: Noise spectral density relation with the gate voltage V_g. Supporting Information Figure S7: Noise spectral density at different frequencies at V_g = −2.0 V. Supporting Information Figure S8: Device responsivity with respect to incident power. Supporting Information Figure S9: Device response on 0 days and 120 days from the first measurement. Description of fabrication, measurements and simulation setup (PDF)

■ AUTHOR INFORMATION

Corresponding Author

Debashis Chanda − *Department of Physics, University of Central Florida, Orlando, Florida 32816, United States; NanoScience Technology Center, University of Central Florida, Orlando, Florida 32826, United States; CREOL, University of Central Florida, Orlando, Florida 32816, United States*; Email: debashis.chanda@ucf.edu

Authors

Tianyi Guo − *Department of Physics, University of Central Florida, Orlando, Florida 32816, United States; NanoScience Technology Center, University of Central Florida, Orlando, Florida 32826, United States; CREOL, University of Central Florida, Orlando, Florida 32816, United States*

Sayan Chandra − *NanoScience Technology Center, University of Central Florida, Orlando, Florida 32826, United States*

Arindam Dasgupta − *NanoScience Technology Center, University of Central Florida, Orlando, Florida 32826, United States*; orcid.org/0000-0001-6160-0788

Muhammad Waqas Shabbir − *NanoScience Technology Center, University of Central Florida, Orlando, Florida 32826, United States*

Aritra Biswas − *Department of Physics, University of Central Florida, Orlando, Florida 32816, United States; NanoScience Technology Center, University of Central Florida, Orlando, Florida 32826, United States; CREOL, University of Central Florida, Orlando, Florida 32816, United States*

Complete contact information is available at: https://pubs.acs.org/10.1021/acs.nanolett.4c03832

Author Contributions

T.G., S.C. and D.C. conceived the idea. T.G., S.C. and A.D. designed and performed the experiments. T.G., S.C., M.W.S. and A.D. analyzed and simulated the data. M.W.S. and D.C. contributed materials/analysis tools. T.G., A.D. and D.C. cowrote the paper. All authors discussed the result and commented on the manuscript.

Funding

This work at the University of Central Florida was supported by e-Skin Displays Inc. under the Extreme Photon Imaging

Capabilities (EPIC) program of Defense Advanced Research Projects Agency (DARPA), grant# HR001122C0045.

Notes

The authors declare no competing financial interest.

■ ACKNOWLEDGMENTS

Authors acknowledges the funding and logistical support of e-Skin Displays Inc. under the Extreme Photon Imaging Capabilities (EPIC) program of the Defense Advanced Research Projects Agency (DARPA), grant# HR001122C0045.

■ REFERENCES

(1) Liu, J.; Xia, F.; Xiao, D.; García de Abajo, F. J.; Sun, D. Semimetals for high-performance photodetection. *Nat. Mater.* **2020**, *19*, 830−837.
(2) Tan, C. L.; Mohseni, H. Emerging technologies for high performance infrared detectors. *Nanophotonics.* **2018**, *7*, 169−197.
(3) Rogalski, A.; Martyniuk, P.; Kopytko, M. Challenges of small-pixel infrared detectors: a review. *Rep. Prog. Phys.* **2016**, *79* (4), 046501.
(4) Russell, T. A.; McMackin, L.; Bridge, B.; Baraniuk, R. *Compressive hyperspectral sensor for LWIR gas detection*; Compressive Sensing, SPIE: 2012; pp 55−67.
(5) Talghader, J. J.; Gawarikar, A. S.; Shea, R. P. Spectral selectivity in infrared thermal detection. *Light Sci. Appl.* **2012**, *1*, No. e24.
(6) Lei, W.; Antoszewski, J.; Faraone, L. Progress, challenges, and opportunities for HgCdTe infrared materials and detectors. *Appl. Phys. Rev.* **2015**, *2*, 041303.
(7) Rogalski, A. HgCdTe infrared detector material: history, status and outlook. *Rep. Prog. Phys.* **2005**, *68*, 2267.
(8) Ferguson, B.; Zhang, X.-C. Materials for terahertz science and technology. *Nat. Mater.* **2002**, *1*, 26−33.
(9) Richards, P. L. Bolometers for infrared and millimeter waves. *J. Appl. Phys.* **1994**, *76*, 1−24.
(10) Zhang, H.; Muhammad, A.; Luo, J.; Tong, Q.; Lei, Y.; Zhang, X.; Sang, H.; Xie, C. MWIR/LWIR filter based on Liquid-Crystal Fabry-Perot structure for tunable spectral imaging detection. *Infrared Phys. Technol.* **2015**, *69*, 68−73.
(11) Neumann, N.; Ebermann, M.; Kurth, S.; Hiller, K. Tunable infrared detector with integrated micromachined Fabry-Perot filter. *J. Micro-Nanolith. MEM.* **2008**, *7*, 021004−021004−9.
(12) Safaei, A.; Chandra, S.; Shabbir, M. W.; Leuenberger, M. N.; Chanda, D. Dirac plasmon-assisted asymmetric hot carrier generation for room-temperature infrared detection. *Nat. Commun.* **2019**, *10*, 3498.
(13) Guo, Q.; Yu, R.; Li, C.; Yuan, S.; Deng, B.; García de Abajo, F. J.; Xia, F. Efficient electrical detection of mid-infrared graphene plasmons at room temperature. *Nat. Mater.* **2018**, *17*, 986−992.
(14) Xia, F.; Farmer, D. B.; Lin, Y.-m.; Avouris, P. Graphene field-effect transistors with high on/off current ratio and large transport band gap at room temperature. *Nano Lett.* **2010**, *10*, 715−718.
(15) Kwong Hong Tsang, D.; Lieberthal, T. J.; Watts, C.; Dunlop, I. E.; Ramadan, S.; del Rio Hernandez, A. E.; Klein, N. Chemically functionalised graphene FET biosensor for the label-free sensing of exosomes. *Sci. Rep.* **2019**, *9*, 13946.
(16) Ergoktas, M. S.; Bakan, G.; Kovalska, E.; Le Fevre, L. W.; Fields, R. P.; Steiner, P.; Yu, X.; Salihoglu, O.; Balci, S.; Fal'ko, V. I. Multispectral graphene-based electro-optical surfaces with reversible tunability from visible to microwave wavelengths. *Nat. Photonics.* **2021**, *15*, 493−498.
(17) Safaei, A.; Chandra, S.; Vázquez-Guardado, A.; Calderon, J.; Franklin, D.; Tetard, L.; Zhai, L.; Leuenberger, M. N.; Chanda, D. Dynamically tunable extraordinary light absorption in monolayer graphene. *Phys. Rev. B* **2017**, *96*, 165431.
(18) Safaei, A.; Chandra, S.; Leuenberger, M. N.; Chanda, D. Wide angle dynamically tunable enhanced infrared absorption on large-area nanopatterned graphene. *ACS Nano* **2019**, *13*, 421−428.
(19) Cakmakyapan, S.; Lu, P. K.; Navabi, A.; Jarrahi, M. Gold-patched graphene nano-stripes for high-responsivity and ultrafast photodetection from the visible to infrared regime. *Light Sci. Appl.* **2018**, *7*, 20.
(20) Kim, B. J.; Jang, H.; Lee, S.-K.; Hong, B. H.; Ahn, J.-H.; Cho, J. H. High-performance flexible graphene field effect transistors with ion gel gate dielectrics. *Nano Lett.* **2010**, *10*, 3464−3466.
(21) Wang, D.; Zhao, S.; Yin, R.; Li, L.; Lou, Z.; Shen, G. Recent advanced applications of ion-gel in ionic-gated transistor. *npj Flex. Electron.* **2021**, *5*, 13.
(22) Oh, G.; Kim, J.-S.; Jeon, J. H.; Won, E.; Son, J. W.; Lee, D. H.; Kim, C. K.; Jang, J.; Lee, T.; Park, B. H. Graphene/pentacene barristor with ion-gel gate dielectric: flexible ambipolar transistor with high mobility and on/off ratio. *ACS Nano* **2015**, *9*, 7515−7522.
(23) Lee, S. W.; Shin, M.; Park, J. Y.; Kim, B. S.; Tu, D.; Jeon, S.; Jeong, U. Thin ion-gel dielectric layer to enhance the stability of polymer transistors. *Sci. Adv. Mater.* **2015**, *7*, 874−880.
(24) Xu, X.; Gabor, N. M.; Alden, J. S.; Van Der Zande, A. M.; McEuen, P. L. Photo-thermoelectric effect at a graphene interface junction. *Nano Lett.* **2010**, *10*, 562−566.
(25) Shautsova, V.; Sidiropoulos, T.; Xiao, X.; Güsken, N. A.; Black, N. C.; Gilbertson, A. M.; Giannini, V.; Maier, S. A.; Cohen, L. F.; Oulton, R. F. Plasmon induced thermoelectric effect in graphene. *Nat. Commun.* **2018**, *9*, 5190.
(26) Gabor, N. M.; Song, J. C.; Ma, Q.; Nair, N. L.; Taychatanapat, T.; Watanabe, K.; Taniguchi, T.; Levitov, L. S.; Jarillo-Herrero, P. Hot carrier-assisted intrinsic photoresponse in graphene. *Science* **2011**, *334*, 648−652.
(27) Yan, H.; Low, T.; Zhu, W.; Wu, Y.; Freitag, M.; Li, X.; Guinea, F.; Avouris, P.; Xia, F. Damping pathways of mid-infrared plasmons in graphene nanostructures. *Nat. Photonics* **2013**, *7*, 394−399.
(28) Buljan, H.; Jablan, M.; Soljačić, M. Damping of plasmons in graphene. *Nat. Photonics.* **2013**, *7*, 346−348.
(29) Harzheim, A.; Spiece, J.; Evangeli, C.; McCann, E.; Falko, V.; Sheng, Y.; Warner, J. H.; Briggs, G. A. D.; Mol, J. A.; Gehring, P.; Kolosov, O. V. Geometrically enhanced thermoelectric effects in graphene nanoconstrictions. *Nano Lett.* **2018**, *18*, 7719−7725.
(30) Sierra, J. F.; Neumann, I.; Costache, M. V.; Valenzuela, S. O. Hot-carrier Seebeck effect: diffusion and remote detection of hot carriers in graphene. *Nano Lett.* **2015**, *15*, 4000−4005.
(31) Ruzicka, B. A.; Wang, S.; Werake, L. K.; Weintrub, B.; Loh, K. P.; Zhao, H. Hot carrier diffusion in graphene. *Phys. Rev. B* **2010**, *82*, 195414.
(32) Fang, Z.; Wang, Y.; Schlather, A. E.; Liu, Z.; Ajayan, P. M.; García de Abajo, F. J.; Nordlander, P.; Zhu, X.; Halas, N. J. Active tunable absorption enhancement with graphene nanodisk arrays. *Nano Lett.* **2014**, *14*, 299−304.
(33) Wang, Q. H.; Jin, Z.; Kim, K. K.; Hilmer, A. J.; Paulus, G. L.; Shih, C.-J.; Ham, M.-H.; Sanchez-Yamagishi, J. D.; Watanabe, K.; Taniguchi, T. Understanding and controlling the substrate effect on graphene electron-transfer chemistry via reactivity imprint lithography. *Nat. Chem.* **2012**, *4*, 724−732.
(34) Gosling, J. H.; Makarovsky, O.; Wang, F.; Cottam, N. D.; Greenaway, M. T.; Patanè, A.; Wildman, R. D.; Tuck, C. J.; Turyanska, L.; Fromhold, T. M. Universal mobility characteristics of graphene originating from charge scattering by ionised impurities. *Commun. Phys.* **2021**, *4*, 30.
(35) Chen, J.-H.; Jang, C.; Adam, S.; Fuhrer, M.; Williams, E. D.; Ishigami, M. Charged-impurity scattering in graphene. *Nat. Phys.* **2008**, *4*, 377−381.
(36) Li, M.-Y.; Tang, C.-C.; Ling, D.; Li, L.; Chi, C.; Chen, J.-C. Charged impurity-induced scatterings in chemical vapor deposited graphene. *J. Appl. Phys.* **2013**, *114* (23). DOI: 10.1063/1.4852435
(37) Van Veldhoven, Z. A.; Alexander-Webber, J. A.; Sagade, A. A.; Braeuninger-Weimer, P.; Hofmann, S. Electronic properties of CVD

https://doi.org/10.1021/acs.nanolett.4c03832
Nano Lett. XXXX, XXX, XXX−XXX

graphene: The role of grain boundaries, atmospheric doping, and encapsulation by ALD. *Phys. Status Solidi B* **2016**, *253*, 2321−2325.
(38) Negishi, R.; Ohno, Y.; Maehashi, K.; Matsumoto, K.; Kobayashi, Y. Carrier transport properties of the field effect transistors with graphene channel prepared by chemical vapor deposition. *Jpn. J. Appl. Phys.* **2012**, *51*, 06FD03.
(39) Zha, J.; Luo, M.; Ye, M.; Ahmed, T.; Yu, X.; Lien, D. H.; He, Q.; Lei, D.; Ho, J. C.; Bullock, J. Infrared photodetectors based on 2D materials and nanophotonics. *Adv. Funct. Mater.* **2022**, *32*, 2111970.
(40) Liu, L.; Liu, Y.; Gong, T.; Huang, W.; Guo, J.; Zhang, X.; Zhou, S.; Yu, B. Graphene-based polarization-sensitive longwave infrared photodetector. *Nanotechnology* **2019**, *30*, 435205.
(41) Rogalski, A. Graphene-based materials in the infrared and terahertz detector families: a tutorial. *Adv. Opt. Photonics.* **2019**, *11*, 314−379.
(42) Vincent, J. D.; Hodges, S.; Vampola, J.; Stegall, M.; Pierce, G. *Fundamentals of Infrared and Visible Detector Operation and Testing*; John Wiley & Sons: 2015.

https://doi.org/10.1021/acs.nanolett.4c03832
Nano Lett. XXXX, XXX, XXX−XXX